

Dual topology and edge-reconstruction in α -Sn

Jan Skolimowski¹,¹ Nguyen Minh Nguyen^{2,1}, Giuseppe Cuono³,³ Carmine Autieri^{1,4}, and Wojciech Brzezicki^{5,1}

¹*International Research Centre Magtop, Institute of Physics,
Polish Academy of Sciences, Aleja Lotników 32/46, PL-02668 Warsaw, Poland*

²*School of Science and Engineering, The Chinese University of Hong Kong, Shenzhen, Shenzhen 518172, China*

³*Consiglio Nazionale delle Ricerche (CNR-SPIN),*

Unità di Ricerca presso Terzi c/o Università “G. D’Annunzio”, 66100 Chieti, Italy

⁴*SPIN-CNR, UOS Salerno, IT-84084 Fisciano (SA), Italy*

⁵*Institute of Theoretical Physics, Jagiellonian University,
ulica S. Łojasiewicza 11, PL-30348 Kraków, Poland*

(Dated: December 1, 2025)

We formulate the tight-binding model for cubic α -Sn based on the DFT calculations. In the model, we incorporate a variable bond angle, which allows us to simulate the effect of the in-plane strain. In the bulk, we demonstrate the presence of the \mathbb{Z}_2 topological invariant and a non-zero mirror Chern number, making α -Sn one of the rare cases where dual topology can be observed. We calculate the topological phase diagram of multi-layer α -Sn as a function of strain and number of layers. We find that a non-trivial quantum spin Hall state appears only for compressive strain above five layers of thickness. Quite surprisingly, both in the trivial and non-trivial phases, we find a plethora of edge-states with energies inside the bulk gap of the system. Some of these states are localized at the side surfaces of the slab, some of them prefer top/bottom surfaces and some are localized in the hinges. We trace the microscopic origin of these states back to a minimal model that supports chiral symmetry and multiple one-dimensional winding numbers that take different values in different directions in the Brillouin zone.

I. INTRODUCTION

α -Sn or gray tin is a semiconducting allotrope of Sn stable at low temperatures. The crystal structure is similar to HgTe (space group No. 216, $F\bar{4}3m$), but since the two atoms of the basis are of the same kind, the α -Sn system (space group No. 227, $Fd\bar{3}m$) presents the inversion symmetry in addition to HgTe. It has garnered significant attention because of its non-trivial band topology^{1–6}. Epitaxial strain can dramatically enhance its stability, allowing thin α -Sn films to persist even at elevated temperatures⁷. Strain not only stabilizes α -Sn but also profoundly reshapes its electronic structure⁸. Compressive in-plane strain, for example, transforms α -Sn into a three-dimensional (3D) Dirac semimetal, as confirmed by ARPES measurements revealing linear surface Dirac cones and spin-momentum-locked topological states⁹ with tunable Dirac points, offering control over novel transport phenomena like negative magnetoresistance¹⁰. Alternatively, tensile in-plane strain can induce a topological insulating phase, which has been less studied experimentally. The interplay of strain, thickness, and spin-orbit coupling leads to topological phase transitions also in the thin films of α -Sn grown along the (111) orientation^{11,12}. Quantum wells of α -Sn under varying strain exhibit switchable topological phases, highlighting its potential in topological and quantum devices. Capping layers such as AlO_x help preserve the topological surface states by maintaining surface integrity¹³. Recent work underscores the strain’s central role in tuning the electronic topology, including the quantum spin Hall phase (QSH), enabling

room-temperature studies of Dirac fermions and quantum oscillations⁹. A large superconducting diode was observed by interfacing the topological α - and the superconducting β -Sn phase¹⁴.

The topological origin of the QSH effect implies the existence of helical edge modes, which are protected against elastic backscattering from all perturbations obeying the time-reversal symmetry. Various materials have been predicted to support the QSH insulator phase^{15–18}. Experimentally, signatures of edge mode transport have been observed in several of the candidate materials, such as HgTe/CdTe quantum wells¹⁹, InAs/GaSb bilayers²⁰, WTe_2 ²¹, bismuthene on SiC²² and Moiré materials²³. However, the experimental studies have also led to discrepancies with the simple theoretical models with protection length of the edge transport reaching only a few tens of nanometers in WTe_2 ²¹, a few micrometers in InAs/GaSb²⁰ and a few tens of micrometers in HgTe/CdTe quantum wells²⁴. There are several possible explanations of this faulty QSH effect, including magnetic impurities²⁵, phonons²⁶, dynamic nuclear polarization^{27,28}, spontaneous time-reversal symmetry breaking^{29–31}, charge puddles³², charge dopants³³ and interaction effects³⁴. A more recent scenario to explain short protection length is the reconstruction of the charge density at the edges^{35–38}, as enhanced edge density of states can trigger local magnetic moment formation. It has been demonstrated that once multiple channels exist³⁷, time reversal symmetry does not forbid scattering between different Kramers pairs³⁹.

In this paper, we use first-principles calculations to derive an effective tight-binding model for α -Sn includ-

ing the effects of lattice strain. After establishing its 3D topological properties, we show that this material supports additional surface states on top and side surfaces of the system, whose number is proportional to the system's height or width, respectively. We trace the microscopic origin of these states back to a minimal model with chiral symmetry and with one-dimensional (1D) winding numbers supporting different numbers of flat bands at different terminations of the system. This limit is achieved when we set onsite energies of the s and p orbitals as the same for all sites and we switch off atomic spin-orbit coupling. We show that the flat bands found in this limit transform smoothly into the additional dispersive edge states found in the spectrum of the full Hamiltonian of α -Sn.

II. TIGHT-BINDING PARAMETERS EXTRACTED FROM FIRST-PRINCIPLES CALCULATIONS

We carried out electronic structure calculations using the VASP package⁴⁰, based on a plane-wave basis set and the projector augmented-wave (PAW) method⁴¹. A plane-wave energy cutoff of 250 eV was adopted for all calculations. The Brillouin zone was sampled using an $8 \times 8 \times 8$ Monkhorst-Pack k -point mesh. In the presence of spin-orbit coupling (SOC), 512 k -points were used within the irreducible Brillouin zone, whereas 176 k -points were utilized in the absence of SOC. For the treatment of exchange-correlation effects, we employed the generalized gradient approximation (GGA) for the exchange-correlation functional.

Because the system is non-magnetic and possesses inversion symmetry, all bands exhibit Kramers degeneracy. At the Γ point, when we include the spin-orbit coupling (SOC), the p -states are separated into the fourfold degenerate Γ_8 and the twofold Γ_7 . The Γ_6 originates from an s -orbital, and the topological nature of the system arises from a band inversion between the Γ_6 and Γ_8 energy levels. Experimentally, Γ_6 is 415 meV below Γ_8 based on ARPES and magnetooptics results⁹. The Γ_7 should be around 800 meV, but we have it at 681 meV below Γ_8 . Within GGA, the band structure does not agree with the experiments since the conduction band at the L point is lower in energy than the Γ_8 state, making the system a metal⁴², while experimentally it is a zero-gap semiconductor. This error of the GGA in the correct representation of bulk band structure is attributed to the usual band-gap problem within DFT and it happens with and without SOC. Using the hybrid functionals HSE⁴³, the meta-GGA functional MBJ¹⁰, or the relativistic self-consistent GW⁴⁴, it has been demonstrated to yield improved agreement with experimental data.

Regarding the tight-binding model, in the literature, we have $k \cdot p$ models and two different sp^3s^* models^{43,45} for α -Sn, which are reported in the Table I. In this paper, we go beyond producing a sp^3 model for α -Sn. In

TABLE I. First-nearest-neighbor tight-binding parameters for cubic diamond α -Sn compared with two previous sp^3s^* tight-binding models^{43,45}. The value of spin-orbit coupling λ was taken from the HSE calculations⁴³, considering that the spin-orbit splitting at Γ is $\Delta_0=3/2\lambda$. All values are in eV.

	This work	sp^3s^* in Ref. 43	sp^3s^* in Ref. 45
E_s	-6.335	-7.2029	-5.8700
E_p	1.104	0.0032	1.3300
E_{s^*}	-	14.1081	5.9000
λ	0.454	0.454	-
$V_{ss\sigma}$	-1.480	-1.4802	-1.4175
$V_{s^*s^*\sigma}$	-	0.4795	-
$V_{sp\sigma}$	1.458	1.9034	1.9536
$V_{s^*p\sigma}$	-	2.7564	2.5522
$V_{pp\sigma}$	2.373	3.3555	2.3725
$V_{pp\pi}$	-0.687	-1.6848	-0.6870

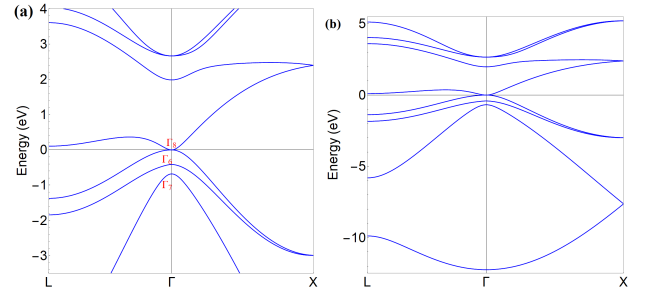


FIG. 1. Relativistic band structure of α -Sn using the tight-binding model reported in Table I. (a) Band structure in the energy range from -3.5 eV to +4 eV. (b) Band structure in an extended energy range. The X-point is at the coordinates $(\frac{1}{2}, 0, 0)$, while the L-point is at the coordinates $(\frac{1}{2}, \frac{1}{2}, \frac{1}{2})$. Γ_8 and Γ_7 represent the p -states at the Γ point while Γ_6 represents the s -state.

the previous sp^3s^* models, we have the presence of the s^* orbital; however, this s^* orbital can be removed without affecting too much the quality of the tight-binding model and simplifying the model. There are two reasons why we can simply do that: the s^* is very high in energy and $V_{s^*p\sigma}$ is the only connection between s^* and the sp^3 orbitals. Indeed, at the Γ point, the sp^3 energetic levels are unaffected by s^* since the eigenvalues at Γ are independent of $V_{s^*p\sigma}$.

Now, we move to extract the tight-binding parameter from the GGA calculations by fitting our band structure at the k -points Γ , X and L following the same procedure described in the literature⁴⁶. In order to fit the experimental values, we renormalize three hopping parameters. We use the parameters $V_{pp\sigma}$ and $V_{pp\pi}$ from the literature⁴⁵. We finally produce our tight-binding by renormalizing $V_{sp\sigma}$ and fitting the experimental information that the conduction band at the L-point is 100 meV above the Fermi level⁹. This procedure decreases the value of $V_{sp\sigma}$, the conduction band at the L point reproduces the experimental results. After shift-

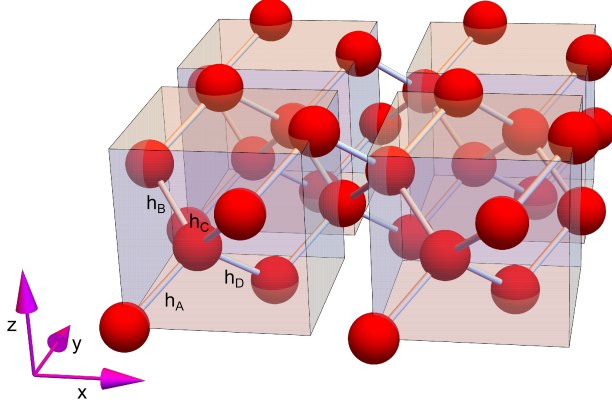


FIG. 2. Schematic illustration of the crystal lattice of α -Sn consisting of two layers of biatomic unit cells stacked along the z -direction. The Sn atoms are represented as balls and nearest-neighbor bonds h_α ($\alpha = A, B, C, D$) as tubes connecting them. Each site supports one s -orbital and three p -orbitals.

ing the energy on-site to have the zero of the energy on the top of the valence band, the results are reported in the first column of Table I. The sign and the size of the tight-binding parameters are the same as those of the previous tight-binding model calculated for other cubic zinc-blended semiconductors^{46,47}.

Using parameters from our tight-binding model, we plot the band structure along the high-symmetry k -path L - Γ - X in Fig. 1 to show the correct behaviour of our results at the L point. Fig. 1(a) shows the low-energy band structure in the range from -3.5 and 4 eV. We can observe how the conduction band at the L point does not cross the Fermi level. In Fig. 1(b), we report the entire energy range where we can observe all the bands obtained within our model. Despite its simplicity, our sp^3 model captures the key topological features of the low-energy band structure of α -Sn.

III. TIGHT-BINDING HAMILTONIAN

Our starting point is a tight-binding Hamiltonian for α -Sn. We consider a primitive unit cell consisting of two Sn atoms at positions $(0,0,0)$ and $(1/2,1/2,1/2)$ and lattice translation vectors being $\vec{n}_1 = (1,1,0)$, $\vec{n}_2 = (-1,1,0)$ and $\vec{n}_3 = (0,1,1)$. The lattice structure is that of a diamond, see Fig. 2. Every Sn atom hosts one s and three p orbitals and we consider hopping only between nearest neighbors. We allow for all hopping processes that preserve spin and use Slater-Koster⁴⁸ parametriza-

tion to write down the hopping matrix in the form of:

$$h_{(l,m,n)} = \begin{pmatrix} V_{ss\sigma} & lV_{sp\sigma} & mV_{sp\sigma} & nV_{sp\sigma} \\ -lV_{sp\sigma} & l^2\delta V + V_{pp\pi} & lm\delta V & ln\delta V \\ -mV_{sp\sigma} & lm\delta V & m^2\delta V + V_{pp\pi} & mn\delta V \\ -nV_{sp\sigma} & ln\delta V & mn\delta V & n^2\delta V + V_{pp\pi} \end{pmatrix}. \quad (1)$$

Where $\delta V = V_{pp\sigma} - V_{pp\pi}$ and where (l, m, n) are direction cosines of a bond along which the electron hops. The parameters $V_{ss\sigma}$, $V_{pp\sigma}$ and $V_{pp\pi}$ are σ - or π -bonding amplitudes between two s or p orbitals, respectively. For NN hopping, we have four possible bond directions that depend on whether the system is strained or not. Here we parametrize the effect of in-plane tensile or compressive strain by introducing the bond angle θ depicted in Fig. 3. Consequently, the bond direction can be expressed by four normalized vectors \vec{A} , \vec{B} , \vec{C} and \vec{D} given by:

$$\begin{aligned} \vec{A}_\theta &= \hat{R}_\theta^{(\bar{1},1,0)} \cdot \vec{e}_z, & \vec{B}_\theta &= \hat{R}_{\pi-\theta}^{(1,1,0)} \cdot \vec{e}_z, \\ \vec{C}_\theta &= \hat{R}_{-\pi+\theta}^{(1,1,0)} \cdot \vec{e}_z, & \vec{D}_\theta &= \hat{R}_{-\theta}^{(\bar{1},1,0)} \cdot \vec{e}_z, \end{aligned} \quad (2)$$

where $\vec{e}_z = (0,0,1)^T$ and $\hat{R}_\theta^{\vec{n}}$ is a θ -rotation operator with respect to the axis \vec{n} . In case of an unstrained, fully symmetric diamond lattice we have $\theta = \theta_0 = \arctan \sqrt{2}$, which yields $\vec{A} = \sqrt{3}^{-1}(1,1,1)$, $\vec{B} = \sqrt{3}^{-1}(1,-1,-1)$, $\vec{C} = \sqrt{3}^{-1}(-1,1,-1)$, $\vec{D} = \sqrt{3}^{-1}(-1,-1,1)$. This angle decreases in the case of compressive strain and increases in the case of tensile strain. Having established the orbital hopping matrices, we can write the full tight-binding Hamiltonian as:

$$\begin{aligned} \mathcal{H}_\theta(\mathbf{k}) &= \mathbb{1}_2 \otimes h_{\vec{A}_\theta} \otimes \begin{pmatrix} 0 & e^{ik_3} \\ 0 & 0 \end{pmatrix} + \mathbb{1}_2 \otimes h_{\vec{B}_\theta} \otimes \begin{pmatrix} 0 & e^{ik_1} \\ 0 & 0 \end{pmatrix} \\ &+ \mathbb{1}_2 \otimes h_{\vec{C}_\theta} \otimes \begin{pmatrix} 0 & 1 \\ 0 & 0 \end{pmatrix} + \mathbb{1}_2 \otimes h_{\vec{D}_\theta} \otimes \begin{pmatrix} 0 & e^{i(k_3-k_2)} \\ 0 & 0 \end{pmatrix} \\ &+ H.c. + \mathbb{1}_2 \otimes E_{\text{orb}} \otimes \mathbb{1}_2 + \lambda \sum_{\alpha=x,y,z} \sigma_\alpha \otimes L_\alpha \otimes \mathbb{1}_2, \end{aligned} \quad (3)$$

where e^{ik_1} , e^{ik_2} and e^{ik_3} are the eigenvalues of the lattice translation operators along lattice vectors \vec{n}_1 , \vec{n}_2 and \vec{n}_3 . To work with Cartesian quasimomenta, we can use a substitution $k_1 = k_x + k_y$, $k_2 = k_y - k_x$, $k_3 = k_y + k_z$.

In the on-site parts of the Hamiltonian, we find E_{orb} being a diagonal 4×4 matrix, describing occupation energies of one s and three p orbitals, with diagonal entries given by $\{E_s, E_p, E_p, E_p\}$. Finally, there is also an atomic spin-orbit coupling with amplitude λ , where σ_α describes electron spin and L_α its orbital degree of freedom. Here, angular-momentum operators have a block-diagonal structure $L_\alpha = L^{(s)} \oplus L_\alpha^{(p)}$ with $L^{(s)} = 0$ being the trivial angular momentum of the s orbital and $L_\alpha^{(p)}$ being $L = 1$ angular momentum of the p orbitals acting on the basis of cubic harmonics p_x , p_y and p_z .

The parameters E_s , E_p , λ , $V_{ss\sigma}$, $V_{pp\pi}$, $V_{ss\sigma}$ of the tight-binding Hamiltonian are given in Table I and have

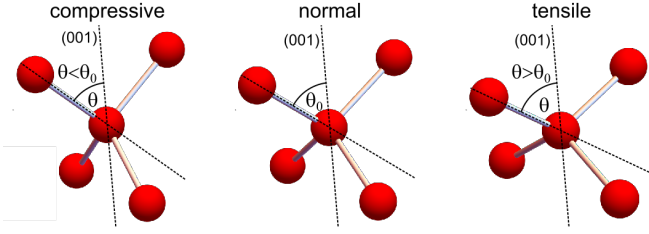


FIG. 3. Schematic illustration of bonds of α -Sn in case of compressive and tensile strain along x and y axes and in case without a strain. In the unstrained case, all bonds are equal, while in the strained case, there are two different sets of bonds.

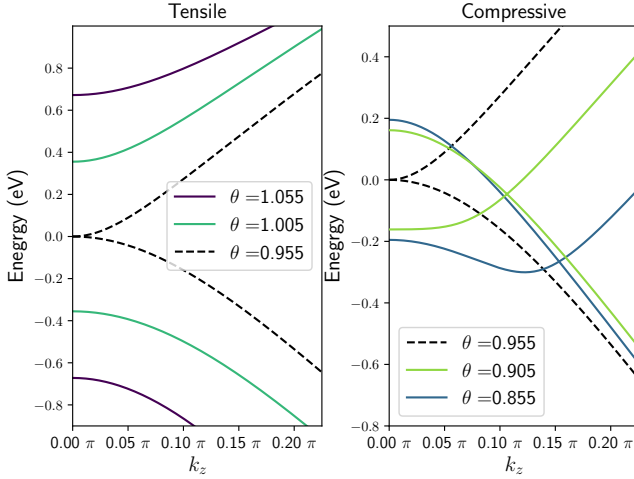


FIG. 4. The response of the bulk band structure around the Γ -point to the tensile (left) and compressive (right) in-plane strain. This strain is modeled as a small change in the polar angle θ of the bond between the sublattices. The unstrained α -Sn bond angle $\theta = \theta_0 = 0.955$ (black dashed line in both panels) serves as a reference. The increase/reduction of θ indicates in-plane stretching/compression of the sample. The comparison indicates that only a compressive strain can induce band inversion at the Γ -point.

been derived from first principles density-functional theory (DFT) calculations. To obtain these parameters with first-neighbour hopping parameters, we impose on the tight-binding model to fit the DFT band structure at high-symmetry points, extracting the on-site energies, the hopping amplitudes and the spin-orbit couplings as fitting parameters.

IV. TOPOLOGICAL PHASE DIAGRAM AND EDGE-STATES

Tensile or compressive strain in the system is controlled by angle θ . In Fig. 4 we show the band structure of the Hamiltonian (4) as a function of k_3 for $k_1 = k_2 = 0$. As expected from earlier studies⁹, the tensile strain opens a gap at half-filling, whereas compressive strain produces

a Dirac point. Therefore, we see that by controlling the strain, we will most likely be able to control the topological phase of the system.

From the point of view of the tenfold Altland-Zirnbauer classification, our system is clearly in the AII class with spin-full time-reversal symmetry. In addition, it also has inversion symmetry \mathcal{I} given by an operator

$$\mathcal{I} = \mathbb{1}_2 \otimes [\mathbb{1}_1 \oplus (-\mathbb{1}_3)] \otimes \tau_x. \quad (4)$$

where τ_x is the x Pauli matrix acting in the sublattice space. From the work of Fu and Kane⁴⁹, we know that in such a case, a \mathbb{Z}_2 invariant of the AII class can be calculated by looking at inversion eigenvalues of the occupied states at the high-symmetry points of the Brillouin zone (BZ), namely

$$(-1)^\nu = \prod_{\vec{K}} \prod_{n \in N_f} \langle \psi_{\vec{K}} | \mathcal{I} | \psi_{\vec{K}} \rangle, \quad (5)$$

where \vec{K} are high-symmetry momenta and $N_f = \{1, 3, \dots, 7\}$ is a set of labels of the occupied states (one from each Kramers doublet, no matter which one) and $\nu = 0, 1$ for the trivial/non-trivial case, respectively. Using this prescription, we can calculate the invariant both in two and three spatial dimensions.

In the 3D case, we find that the system is always in a topological insulator phase with $\nu = 1$ as long as the tensile strain is applied. In the unstrained case, there is a parabolic band-touching at Γ point which evolves into two linear band-crossings present at $\vec{k} = (0, 0, \pm\xi_z)$ for any compressive strain (see Fig. 4). Interestingly, while the system remains gapless in this limit, the ν invariant does not change with respect to the topological phase. Finally, we have also found that in the tensile strain case, the system realizes a topological crystalline insulator phase with a (110)-mirror Chern number $C = 1$. This is a similar behavior to the one exhibited by SnTe-class compounds^{50,51}, which suggests that the Dirac cones found at the surface of α -Sn¹³ can survive breaking of the time-reversal symmetry as long as the mirror symmetry is preserved. In such a case, they would move away from the high-symmetry positions.

In the two-dimensional case, which is the main focus of this work, we are interested in a quantum-well configuration of α -Sn, so we will stack a given number of layers of α -Sn in the direction of \vec{n}_3 . The topological phase diagram as a function of the number of layers and the angle θ is given in Fig. 5. As we can see, first of all, the system does not always stay insulating and this depends mainly on θ . We clearly see the window of θ starting roughly at $0.9\theta_0$ and ending roughly at $1.01\theta_0$, where the system has a direct gap for any number of layers. Below 15 layers, this window extends more to the lower values of θ , apart from a single-layer case, which remains gapped for any angle θ considered here. The non-trivial phase appears $\theta < \theta_0$, as long as there is more than one layer of the system, and it takes a slightly weird shape of finger-like

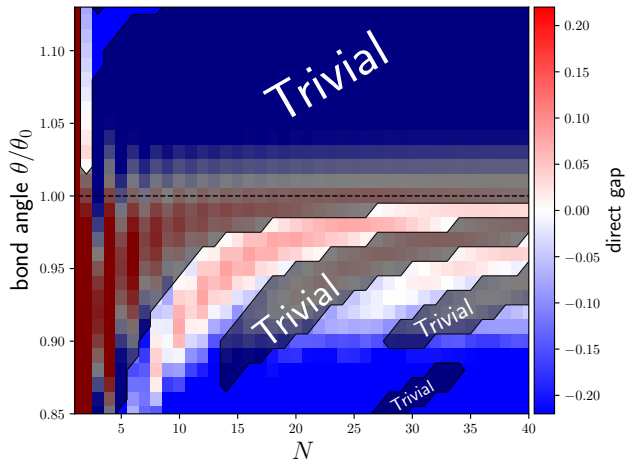


FIG. 5. Phase diagram of a layered α -Sn system. On the horizontal axis is N , the number of layers along the \vec{n}_3 direction. On the vertical axis is the bond polar angle between the sublattices divided by the unstrained angle θ_0 . Values larger (smaller) than one indicate tensile (compressive) in-plane strain. The color scheme denotes the value of the direct gap between the conduction and valence bands at the high-symmetry points. The blue and white regions are regions without a direct gap. The additional dark shading represents the regions where the system is topologically trivial.

fringes that get narrower as the number of layers grows, consistently with the 3D properties of the system.

Having established the topological phase diagram, we can now examine the edge states. In Fig. 6, we show the band structures around the Fermi level in the case of 10 layers of the system with open edge parallel to the \vec{n}_2 direction. We present the reference case with no strain, as well as small compressive and larger compressive strains. However, what is interesting here is that according to the phase diagram, we should only see the in-gap edge-states in the last case, but we observe them in all cases. Looking at the spatial projections of these states, we clearly see that they are all strongly localized at the edges, especially for $k_2 = \pi$, where the bulk gap is the largest (some of the states also prefer to stay more on top/bottom layers rather than in the central ones). We also note that these states are typically not connecting the valence and conduction bands - only in the larger-compressive-strain case, which is supposed to support the \mathbb{Z}_2 invariant, we see a pair of helical states which connect through the bulk gap.

Summarizing, the situation with the edge-state here is similar to the one encountered in the HgTe/CdTe quantum wells³⁷; however, we are dealing with an inversion-symmetric system that is also homogeneous along the stacking direction.

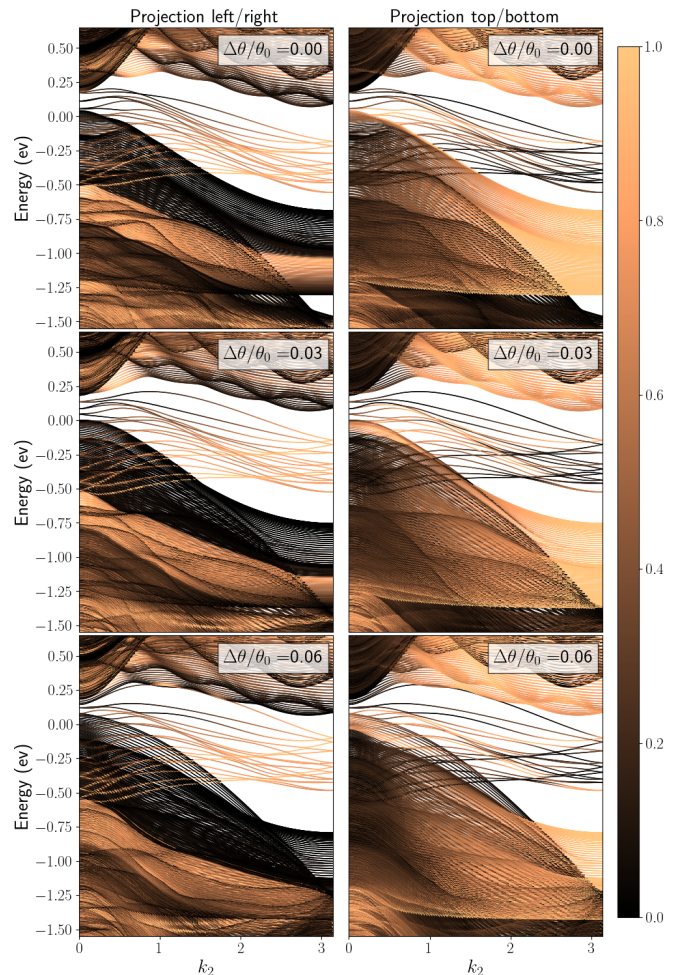


FIG. 6. Band structure of a slab with $N_z = 10$ and $N_x = 80$ with the colors representing the projection of each band on the left/right (left) and top/bottom (right) surfaces of the slab. In each row, the results for a certain compressive strain ($\Delta\theta = \theta_0 - \theta$), denoted in the top right corner, are shown. The same color scale, explained on the right side of the figure, is used in each panel.

V. HIDDEN WINDING NUMBERS

Our task now is to understand the origin of the additional edge-states shown in Fig. 6. This can be achieved by continuously evolving the Hamiltonian to a point where it has more symmetries. Based on an educated guess, given earlier works showing that the diamond lattice can support 1D winding numbers⁵², we choose the direction of this evolution to be towards a chiral-symmetric system. This can be obtained by setting:

$$E_p = E_s, \quad \lambda = 0, \quad (6)$$

and subtracting the constant energy shift of E_s , i.e.,

$$\mathcal{H}_{\text{chir}}(\mathbf{k}) = \mathcal{H}_{\theta_0}(\mathbf{k}, E_p = E_s, \lambda = 0) - E_s \mathbf{1}_{16}. \quad (7)$$

Note that in this Section, we will focus on the unstrained case of $\theta = \theta_0$ for the sake of simplicity, but the reasoning

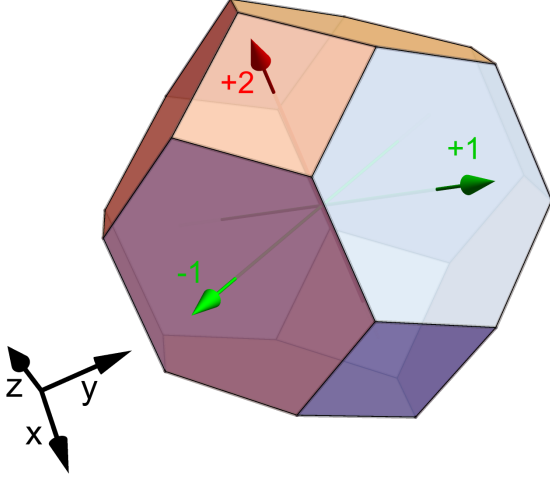


FIG. 7. Diamond-lattice Brillouin zone with marked 1D winding numbers ν_{1D} calculated along directions indicated by red and green arrows.

stays valid for any other θ . From the fact that the diamond lattice is bipartite and the Hamiltonian contains only NN hopping, it is easy to infer that $\mathcal{H}_{\text{chir}}(\mathbf{k})$ has a sublattice or chiral symmetry given by

$$\mathcal{S} = \mathbb{1}_2 \otimes \mathbb{1}_4 \otimes \begin{pmatrix} 1 & 0 \\ 0 & -1 \end{pmatrix}, \quad (8)$$

satisfying $\{\mathcal{H}_{\text{chir}}(\mathbf{k}), \mathcal{S}\} \equiv 0$. From this it follows that we can block-off-diagonalize $\mathcal{H}_{\text{chir}}(\mathbf{k})$ in the eigenbasis of \mathcal{S} . Additionally, since we have turned off the spin-orbit coupling, the spin channels are now decoupled, so we can consider only the spin-up Hamiltonian. Thus, we have:

$$\mathcal{H}_{\text{chir}}^{\uparrow}(\mathbf{k}) = \begin{pmatrix} 0 & u_{\mathbf{k}} \\ u_{\mathbf{k}}^{\dagger} & 0 \end{pmatrix}, \quad (9)$$

where

$$u_{\mathbf{k}} = \begin{pmatrix} q_{\mathbf{k}}^{(1)} \frac{V_{ss\sigma}}{\sqrt{3}} & q_{\mathbf{k}}^{(2)} \frac{V_{sp\sigma}}{\sqrt{3}} & -q_{\mathbf{k}}^{(3)} \frac{V_{sp\sigma}}{\sqrt{3}} & -q_{\mathbf{k}}^{(4)} \frac{V_{sp\sigma}}{\sqrt{3}} \\ -q_{\mathbf{k}}^{(2)} \frac{V_{sp\sigma}}{\sqrt{3}} & q_{\mathbf{k}}^{(1)} \frac{V_{+}}{3} & q_{\mathbf{k}}^{(4)} \frac{V_{-}}{3} & q_{\mathbf{k}}^{(3)} \frac{V_{-}}{3} \\ q_{\mathbf{k}}^{(3)} \frac{V_{sp\sigma}}{\sqrt{3}} & q_{\mathbf{k}}^{(4)} \frac{V_{-}}{3} & q_{\mathbf{k}}^{(1)} \frac{V_{+}}{3} & -q_{\mathbf{k}}^{(2)} \frac{V_{-}}{3} \\ q_{\mathbf{k}}^{(4)} \frac{V_{sp\sigma}}{\sqrt{3}} & q_{\mathbf{k}}^{(3)} \frac{V_{-}}{3} & -q_{\mathbf{k}}^{(2)} \frac{V_{-}}{3} & q_{\mathbf{k}}^{(1)} \frac{V_{+}}{3} \end{pmatrix}, \quad (10)$$

and

$$V_{+} = 2V_{pp\pi} + V_{pp\sigma}, \quad V_{-} = V_{pp\pi} - V_{pp\sigma}, \quad (11)$$

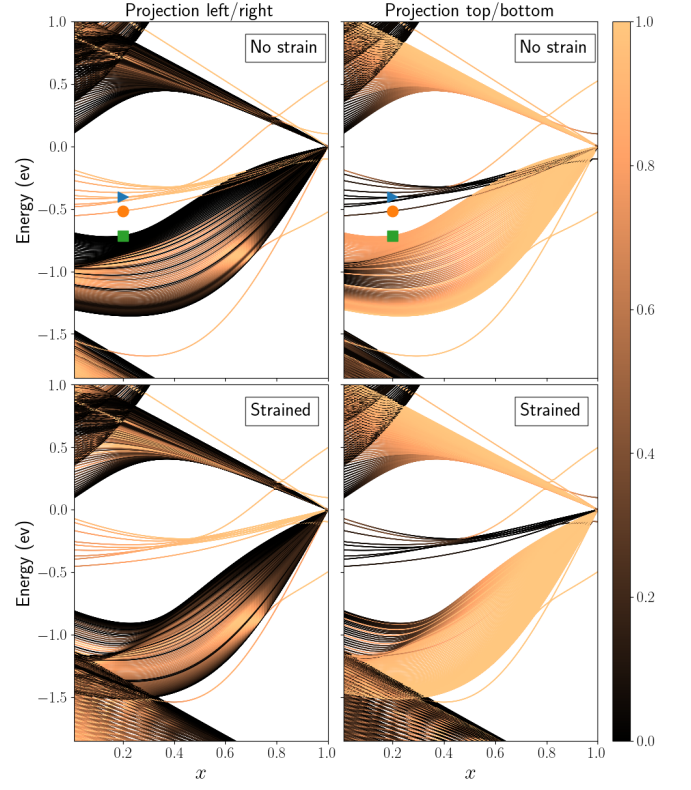


FIG. 8. Band structure at $k_2 = \pi$ of unstrained (top) and strained (bottom) slab of α -tin model with $N_3 = 10$ and $N_1 = 80$ as the parameters evolve from the experimental values ($x = 0$) to the chiral effective model ($x = 1$). The color scale, explained on the right side, describes the projection of the spectral weight of each band at the left/right (left column) and top/bottom (right column) termination surfaces. The blue triangles, orange circles, and green squares denote specific in-gap states that will be examined later.

as well as:

$$\begin{aligned} q_{\mathbf{k}}^{(1)} &= 1 + e^{ik_1} + e^{ik_3} + e^{i(k_3-k_2)}, \\ q_{\mathbf{k}}^{(2)} &= -1 + e^{ik_1} + e^{ik_3} - e^{i(k_3-k_2)}, \\ q_{\mathbf{k}}^{(3)} &= -1 + e^{ik_1} - e^{ik_3} + e^{i(k_3-k_2)}, \\ q_{\mathbf{k}}^{(4)} &= 1 + e^{ik_1} - e^{ik_3} - e^{i(k_3-k_2)}. \end{aligned} \quad (12)$$

The Hamiltonian $\mathcal{H}_{\text{chir}}^{\uparrow}$ is clearly of the BDI class, so it can support a chiral \mathbb{Z} invariant in three dimensions or weaker chiral \mathbb{Z} invariants (winding numbers) living in the 1D cuts of 3D BZ. It turns out that the latter case is the one that is indeed realized and it is quite intriguing. We find that the values of the winding numbers depend on the direction in the BZ. In Fig. 7 we show the diamond-lattice BZ with different winding numbers ν_{1D} indicated depending on the chosen direction (note that we use Cartesian $k_{x,y,z}$ here). We observe that if we decide to go along the four-fold rotation axes, we always get $\nu_{1D} = 2$, but if we go along the six-fold rotation axes,

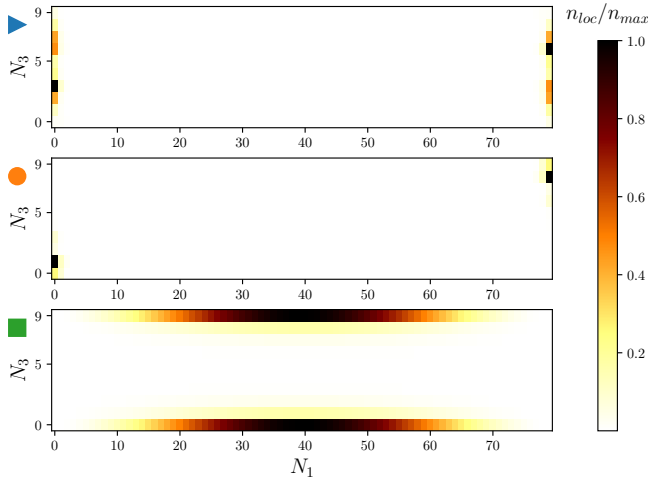


FIG. 9. Local density of electrons (normalized to the maximal value) across the unstrained slab of $N_3 = 10$ and $N_1 = 80$ and parameter $x = 0.2$ for various in-gap states at $k_2 = \pi$. The in-gap states are indicated by blue triangles, orange circles, and green squares in Fig. 8.

it takes values ± 1 depending on which axis we choose. This is clearly related to the fact that different ending surfaces can either consist of atoms belonging only to one sublattice (in the case of six-fold rotation-invariant surfaces) or to both (in the case of four-fold rotation-invariant surfaces). Finally, to prove the relevance of the chiral model to the original one, we show in Fig. 8 the evolution of the band structure at $k_2 = \pi$ of a system with an open edge upon linear interpolation between the full and the chiral symmetric Hamiltonian. The interpolation parameter is x and for $x = 0$ we have a full model and for $x = 1$ the chiral effective one, so with $E_p = E_s$ and $\lambda = 0$. We see that our edge-states smoothly evolve into a flat band at $E = 0$ whose existence follows from a non-zero winding number. Note that some of the valence and conduction states also join the flat band and these are the ones that are localized at the top/bottom surfaces. This follows from the fact that both left/right and top/bottom surfaces have related winding numbers that lead to zero-energy states localized at these surfaces. This also allows us to predict how many additional edge-states we get in the original system, depending on the number of layers.

The spatial profile of different kinds of edge-states shown in Fig. 8 is given in Fig. 9. Quite surprisingly, we still see that apart from states localized on the left/right or top/bottom surfaces, we also get some resembling hinge-states. In the case of the slab considered here, however, the lack of any spatial symmetry excludes the existence of rigorous higher-order topological states. We suspect that their presence is related to the mirror Chern number, like that of SnTe^{53} , which can lead to topological hinge states when the hinge is compatible with mirror symmetry. We also note that these non-exact hinge-states do not join the flat band at $x = 1$, so

they are not related to the winding numbers.

VI. CONCLUSIONS

We have shown within a simple tight-binding model that multilayers of α -Sn can host a QSH phase when compressive strain is applied and this phase depends on the number of layers. Similarly, as discovered in HgTe/CdTe quantum wells³⁷, both in the trivial and non-trivial phases, we obtain additional edge states within the energy gap when the edges of the 2D multilayer system are open. Such states could lead to multimode edge-transport, distorting the sought-after quantum spin Hall effect. These additional edge-states do not follow from any rigorous topological invariant; however, we find the limit of the model within which they follow from the winding numbers present in the 1D cuts of the 3D BZ. It is reached by setting spin-orbit coupling to zero and removing crystal-field splitting between s and p orbitals. In this limit, the system becomes chiral-symmetric and the additional edge-states become zero-energy flat-bands localized on top/bottom or the left-right surfaces of the slab, depending on a particular value of the winding number in a given direction. Quite surprisingly, when the system is tuned towards the chiral limit, we find isolated cases of edge-states that do not join flat bands but remain at finite energy. Their local densities tend to localize at the hinges of the slab, which may be a relic of the presence of the mirror Chern numbers that we find in the 3D limit of the model. The presence of the \mathbb{Z}_2 invariant and a non-zero mirror Chern number makes the present system one of the rare cases where dual topology can be observed.

The transition from a Dirac semimetal to the QSH phase when the system's dimensionality is reduced, from three to two, could also be realized in other material systems. Since thickness-dependent investigation of α -Sn poses experimental challenges, similar physics might be more accessible in van der Waals materials, where exfoliation techniques can be readily applied. In this context, we identify PtSe_2 and PtTe_2 (space group No. 164) as promising candidates to host the QSH phase. These compounds have been reported to exhibit a 3D topological-insulator phase in the bulk and to evolve into normal insulators in the monolayer limit.^{54–56} Our theoretical results further suggest that intermediate-thickness films of these materials could host the QSH phase.

ACKNOWLEDGMENTS

We thank D. Zgid, T. Dietl, J. Polaczyński, A. Kazakov and V. V. Volobuev for their useful discussions. This research was supported by the Foundation for Polish Sci-

ence project “MagTop” no. FENG.02.01-IP.05-0028/23 co-financed by the European Union from the funds of Priority 2 of the European Funds for a Smart Economy Program 2021–2027 (FENG). G.C. and C.A. acknowledge support from PNRR MUR project PE0000023-NQSTI. W.B., J.S. and N.M.N. acknowledge support by Narodowe Centrum Nauki (NCN, National Science Centre, Poland) Project No. 2019/34/E/ST3/00404. We ac-

knowledge the access to the computing facilities of the Interdisciplinary Center of Modeling at the University of Warsaw, Grant G84-0, GB84-1 and GB84-7. We acknowledge the CINECA award under the ISCRA initiative IsC85 ”TOPMOST” and IsC93 ”RATIO” grant, for the availability of high-performance computing resources and support. We acknowledge the access to the computing facilities of the Poznan Supercomputing and Networking Center, Grant No. 609.

- ¹ J.-C. Rojas-Sánchez, S. Oyarzún, Y. Fu, A. Marty, C. Vergnaud, S. Gambarelli, L. Vila, M. Jamet, Y. Ohtsubo, A. Taleb-Ibrahimi, P. Le Fèvre, F. Bertran, N. Reyren, J.-M. George, and A. Fert, “Spin to charge conversion at room temperature by spin pumping into a new type of topological insulator: α -Sn films,” *Phys. Rev. Lett.* **116**, 096602 (2016).
- ² Le Duc Anh, Kengo Takase, Takahiro Chiba, Yohei Kota, Kosuke Takiguchi, and Masaaki Tanaka, “Elemental topological dirac semimetal α -Sn with high quantum mobility,” *Advanced Materials* **33**, 2104645 (2021).
- ³ Yoshiyuki Ohtsubo, Patrick Le Fèvre, Fran çois Bertran, and Amina Taleb-Ibrahimi, “Dirac cone with helical spin polarization in ultrathin α -Sn(001) films,” *Phys. Rev. Lett.* **111**, 216401 (2013).
- ⁴ A. Barfuss, L. Dudy, M. R. Scholz, H. Roth, P. Höpfner, C. Blumenstein, G. Landolt, J. H. Dil, N. C. Plumb, M. Radovic, A. Bostwick, E. Rotenberg, A. Fleszar, G. Bihlmayer, D. Wortmann, G. Li, W. Hanke, R. Claessen, and J. Schäfer, “Elemental topological insulator with tunable Fermi level: Strained α -Sn on InSb(001),” *Phys. Rev. Lett.* **111**, 157205 (2013).
- ⁵ Aaron N. Engel, Connor P. Dempsey, Hadass S. Inbar, Jason T. Dong, Shinichi Nishihaya, Yuhao Chang, Alexei V. Fedorov, Makoto Hashimoto, Donghui Lu, and Christopher J. Palmström, “Growth and characterization of α -Sn thin films on In- and Sb-rich reconstructions of InSb(001),” *Phys. Rev. Mater.* **8**, 044202 (2024).
- ⁶ K. H. M. Chen, K. Y. Lin, S. W. Lien, S. W. Huang, C. K. Cheng, H. Y. Lin, C.-H. Hsu, T.-R. Chang, C.-M. Cheng, M. Hong, and J. Kwo, “Thickness-dependent topological phase transition and Rashba-like preformed topological surface states of α -Sn(001) thin films on InSb(001),” *Phys. Rev. B* **105**, 075109 (2022).
- ⁷ Huanhuan Song, Jinshan Yao, Yuanfeng Ding, Yu Gu, Yu Deng, Ming-Hui Lu, Hong Lu, and Yan-Feng Chen, “Thermal stability enhancement in epitaxial α tin films by strain engineering,” *Advanced Engineering Materials* **21**, 1900410 (2019).
- ⁸ Huaqing Huang and Feng Liu, “Tensile strained gray tin: Dirac semimetal for observing negative magnetoresistance with Shubnikov–de Haas oscillations,” *Phys. Rev. B* **95**, 201101 (2017).
- ⁹ Jakub Polaczyński, Gauthier Krizman, Alexandr Kazakov, Bartłomiej Turowski, Joaquín Bermejo Ortiz, Rafał Rudniewski, Tomasz Wojciechowski, Piotr Dłużewski, Marta Aleszkiewicz, Wojciech Zaleszczyk, Bogusława Kurowska, Zahir Muhammad, Marcin Rosmus, Natalia Olszowska, Louis-Anne de Vaultier, Yves Guldner, Tomasz Wojtowicz, and Valentine V. Volobuev, “3d topological semimetal phases of strained α -Sn on insulating substrate,” *Materials Today* **75**, 135–148 (2024).
- ¹⁰ Md Shahin Alam, Alexandr Kazakov, Mujeeb Ahmad, Rajibul Islam, Fei Xue, and Marcin Matusiak, “Quantum transport properties of the topological Dirac semimetal α -sn,” *Phys. Rev. B* **109**, 245135 (2024).
- ¹¹ Zhibin Shi, Xiaoxiong Wang, Caizhi Xu, Peng Wang, Yang Liu, and T.-C. Chiang, “First-principles study of the topological surface states of α -Sn(111),” *Physics Letters A* **384**, 126782 (2020).
- ¹² V. A. Rogalev, F. Reis, F. Adler, M. Bauernfeind, J. Erhardt, A. Kowalewski, M. R. Scholz, L. Dudy, L. B. Duffy, T. Hesjedal, M. Hoesch, G. Bihlmayer, J. Schäfer, and R. Claessen, “Tailoring the topological surface state in ultrathin α -Sn(111) films,” *Phys. Rev. B* **100**, 245144 (2019).
- ¹³ Quentin Barbedienne, Julien Varignon, Nicolas Reyren, Alain Marty, Céline Vergnaud, Matthieu Jamet, Carmen Gomez-Carbonell, Aristide Lemaître, Patrick Le Fèvre, Fran çois Bertran, Amina Taleb-Ibrahimi, Henri Jaffrès, Jean-Marie George, and Albert Fert, “Angular-resolved photoemission electron spectroscopy and transport studies of the elemental topological insulator α -Sn,” *Phys. Rev. B* **98**, 195445 (2018).
- ¹⁴ Le Duc Anh, Keita Ishihara, Tomoki Hotta, Kohdai Inagaki, Hideki Maki, Takahiro Saeki, Masaki Kobayashi, and Masaaki Tanaka, “Large superconducting diode effect in ion-beam patterned Sn-based superconductor nanowire/topological Dirac semimetal planar heterostructures,” *Nature Communications* **15** (2024), 10.1038/s41467-024-52080-4.
- ¹⁵ M. Z. Hasan and C. L. Kane, “Colloquium: Topological insulators,” *Rev. Mod. Phys.* **82**, 3045–3067 (2010).
- ¹⁶ Xiao-Liang Qi and Shou-Cheng Zhang, “Topological insulators and superconductors,” *Rev. Mod. Phys.* **83**, 1057–1110 (2011).
- ¹⁷ B. Andrei Bernevig, Taylor L. Hughes, and Shou-Cheng Zhang, “Quantum Spin Hall Effect and Topological Phase Transition in HgTe Quantum Wells,” *Science* **314**, 1757–1761 (2006).
- ¹⁸ Chaoxing Liu, Taylor L. Hughes, Xiao-Liang Qi, Kang Wang, and Shou-Cheng Zhang, “Quantum Spin Hall Effect in Inverted Type-II Semiconductors,” *Phys. Rev. Lett.* **100**, 236601 (2008).
- ¹⁹ Markus König, Steffen Wiedmann, Christoph Brüne, Andreas Roth, Hartmut Buhmann, Laurens W. Molenkamp, Xiao-Liang Qi, and Shou-Cheng Zhang, “Quantum Spin Hall Insulator State in HgTe Quantum Wells,” *Science* **318**, 766–770 (2007).

- ²⁰ Lingjie Du, Ivan Knez, Gerard Sullivan, and Rui-Rui Du, “Robust Helical Edge Transport in Gated InAs/GaSb Bilayers,” *Phys. Rev. Lett.* **114**, 096802 (2015).
- ²¹ Sanfeng Wu, Valla Fatemi, Quinn D. Gibson, Kenji Watanabe, Takashi Taniguchi, Robert J. Cava, and Pablo Jarillo-Herrero, “Observation of the quantum spin Hall effect up to 100 Kelvin in a monolayer crystal,” *Science* **359**, 76–79 (2018).
- ²² F. Reis, G. Li, L. Dudy, M. Bauernfeind, S. Glass, W. Hanke, R. Thomale, J. Schäfer, and R. Claessen, “Bismuthene on a SiC substrate: A candidate for a high-temperature quantum spin Hall material,” *Science* **357**, 287–290 (2017), <https://www.science.org/doi/pdf/10.1126/science.aai8142>.
- ²³ Kaifei Kang, Bowen Shen, Yichen Qiu, Yihang Zeng, Zhengchao Xia, Kenji Watanabe, Takashi Taniguchi, Jie Shan, and Kin Fai Mak, “Evidence of the fractional quantum spin Hall effect in moiré MoTe₂,” *Nature* **628**, 522–526 (2024).
- ²⁴ Lukas Lunczer, Philipp Leubner, Martin Endres, Valentin L. Müller, Christoph Brüne, Hartmut Buhmann, and Laurens W. Molenkamp, “Approaching Quantization in Macroscopic Quantum Spin Hall Devices through Gate Training,” *Phys. Rev. Lett.* **123**, 047701 (2019).
- ²⁵ Yoichi Tanaka, A. Furusaki, and K. A. Matveev, “Conductance of a helical edge liquid coupled to a magnetic impurity,” *Phys. Rev. Lett.* **106**, 236402 (2011).
- ²⁶ Jan Carl Budich, Fabrizio Dolcini, Patrik Recher, and Björn Trauzettel, “Phonon-induced backscattering in helical edge states,” *Phys. Rev. Lett.* **108**, 086602 (2012).
- ²⁷ Anders Mathias Lunde and Gloria Platero, “Helical edge states coupled to a spin bath: Current-induced magnetization,” *Phys. Rev. B* **86**, 035112 (2012).
- ²⁸ Adrian Del Maestro, Timo Hyart, and Bernd Rosenow, “Backscattering between helical edge states via dynamic nuclear polarization,” *Phys. Rev. B* **87**, 165440 (2013).
- ²⁹ D. I. Pikulin and T. Hyart, “Interplay of Exciton Condensation and the Quantum Spin Hall Effect in InAs/GaSb Bilayers,” *Phys. Rev. Lett.* **112**, 176403 (2014).
- ³⁰ Tania Paul, V. Fernández Becerra, and Timo Hyart, “Interplay of quantum spin Hall effect and spontaneous time-reversal symmetry breaking in electron-hole bilayers. I. transport properties,” *Phys. Rev. B* **106**, 235420 (2022).
- ³¹ Tania Paul, V. Fernández Becerra, and Timo Hyart, “Interplay of quantum spin Hall effect and spontaneous time-reversal symmetry breaking in electron-hole bilayers. II. zero-field topological superconductivity,” *Phys. Rev. B* **106**, 235421 (2022).
- ³² Jukka I. Väyrynen, Moshe Goldstein, Yuval Gefen, and Leonid I. Glazman, “Resistance of helical edges formed in a semiconductor heterostructure,” *Phys. Rev. B* **90**, 115309 (2014).
- ³³ Tomasz Dietl, “Effects of charge dopants in quantum spin Hall materials,” *Phys. Rev. Lett.* **130**, 086202 (2023).
- ³⁴ G. Dolcetto, M. Sassetti, and T. L. Schmidt, “Edge physics in two-dimensional topological insulators,” *La Rivista del Nuovo Cimento* **39**, 113–154 (2016).
- ³⁵ Jianhui Wang, Yigal Meir, and Yuval Gefen, “Spontaneous breakdown of topological protection in two dimensions,” *Phys. Rev. Lett.* **118**, 046801 (2017).
- ³⁶ A. Amaricci, L. Privitera, F. Petocchi, M. Capone, G. Sangiovanni, and B. Trauzettel, “Edge state reconstruction from strong correlations in quantum spin Hall insulators,” *Phys. Rev. B* **95**, 205120 (2017).
- ³⁷ Nguyen Minh Nguyen, Giuseppe Cuono, Rajibul Islam, Carmine Autieri, Timo Hyart, and Wojciech Brzezicki, “Unprotected edge modes in quantum spin Hall insulator candidate materials,” *Phys. Rev. B* **107**, 045138 (2023).
- ³⁸ Rahul Soni, Matthias Thamm, Gonzalo Alvarez, Bernd Rosenow, and Adrian Del Maestro, “Edge reconstruction in a quantum spin Hall insulator,” (2025), arXiv:2508.10726 [cond-mat.mes-hall].
- ³⁹ Jonas Erhardt, Mattia Iannetti, Fernando Dominguez, Ewelina M. Hankiewicz, Björn Trauzettel, Gianni Profeta, Domenico Di Sante, Giorgio Sangiovanni, Simon Moser, and Ralph Claessen, “Backscattering in topological edge states despite time-reversal symmetry,” *Nature Communications* **16**, 8209 (2025).
- ⁴⁰ G. Kresse and J. Furthmüller, “Efficiency of ab-initio total energy calculations for metals and semiconductors using a plane-wave basis set,” *Comput. Mat. Sci.* **6**, 15–50 (1996).
- ⁴¹ G. Kresse and D. Joubert, “From ultrasoft pseudopotentials to the projector augmented-wave method,” *Phys. Rev. B* **59**, 1758–1775 (1999).
- ⁴² Materials Project, “Materials data on Sn (mp-117) by materials project,” <https://next-gen.materialsproject.org/materials/mp-117?chemsys=Sn> (2025), accessed July 11, 2025.
- ⁴³ Sebastian Küfner, Jürgen Furthmüller, Lars Matthes, Martin Fitzner, and Friedhelm Bechstedt, “Structural and electronic properties of α -tin nanocrystals from first principles,” *Phys. Rev. B* **87**, 235307 (2013).
- ⁴⁴ G. Harsha, S. Dirnboeck, E. Gull, V. Vlcek, and D. Zgid, Private communication. (2026).
- ⁴⁵ P. Vogl, Harold P. Hjalmarson, and John D. Dow, “A semi-empirical tight-binding theory of the electronic structure of semiconductors,” *Journal of Physics and Chemistry of Solids* **44**, 365–378 (1983).
- ⁴⁶ Carmine Autieri, Cezary Śliwa, Rajibul Islam, Giuseppe Cuono, and Tomasz Dietl, “Momentum-resolved spin splitting in Mn-doped trivial CdTe and topological HgTe semiconductors,” *Phys. Rev. B* **103**, 115209 (2021).
- ⁴⁷ Nguyen Minh Nguyen, Giuseppe Cuono, Rajibul Islam, Carmine Autieri, Timo Hyart, and Wojciech Brzezicki, “Unprotected edge modes in quantum spin Hall insulator candidate materials,” *Phys. Rev. B* **107**, 045138 (2023).
- ⁴⁸ J. C. Slater and G. F. Koster, “Simplified lcao method for the periodic potential problem,” *Phys. Rev.* **94**, 1498–1524 (1954).
- ⁴⁹ Liang Fu and C. L. Kane, “Topological insulators with inversion symmetry,” *Phys. Rev. B* **76**, 045302 (2007).
- ⁵⁰ P. Dziawa, B. J. Kowalski, K. Dybko, R. Buczko, A. Szczerbakow, M. Szot, E. Lusakowska, T. Balasubramanian, B. M. Wojek, M. H. Berntsen, O. Tjernberg, and T. Story, “Topological crystalline insulator states in Pb_{1-x}Sn_xSe,” *Nature Materials* **11**, 1023 (2012).
- ⁵¹ Y. Tanaka, Zhi Ren, T. Sato, K. Nakayama, S. Souma, T. Takahashi, Kouji Segawa, and Yoichi Ando, “Experimental realization of a topological crystalline insulator in SnTe,” *Nature Physics* **8**, 800 (2012).
- ⁵² Ryuji Takahashi and Shuichi Murakami, “Completely flat bands and fully localized states on surfaces of anisotropic diamond-lattice models,” *Phys. Rev. B* **88**, 235303 (2013).
- ⁵³ Frank Schindler, Ashley M. Cook, Maia G. Vergniory, Zhi-jun Wang, Stuart S. P. Parkin, B. Andrei Bernevig, and Titus Neupert, “Higher-order topological in-

- sulators,” *Science Advances* **4**, eaat0346 (2018), <https://www.science.org/doi/pdf/10.1126/sciadv.aat0346>.
- ⁵⁴ Mingzhe Yan, Huaqing Huang, Kenan Zhang, Eryin Wang, Wei Yao, Ke Deng, Guoliang Wan, Hongyun Zhang, Masashi Arita, Haitao Yang, Zhe Sun, Hong Yao, Yang Wu, Shoushan Fan, Wenhui Duan, and Shuyun Zhou, “Lorentz-violating type-II Dirac fermions in transition metal dichalcogenide PtTe₂,” *Nature Communications* **8**, 257 (2017).
- ⁵⁵ Huaqing Huang, Shuyun Zhou, and Wenhui Duan, “Type-II Dirac fermions in the PtSe₂ class of transition metal dichalcogenides,” *Phys. Rev. B* **94**, 121117 (2016).
- ⁵⁶ Kenan Zhang, Mingzhe Yan, Haoxiong Zhang, Huaqing Huang, Masashi Arita, Zhe Sun, Wenhui Duan, Yang Wu, and Shuyun Zhou, “Experimental evidence for type-II Dirac semimetal in PtSe₂,” *Phys. Rev. B* **96**, 125102 (2017).